# Mechanisms of incursion accommodation during interaction between a vibrating blade and an abradable coating

Romain Mandard, Yannick Desplanques, Grégory Hauss, Jacky Fabis, Jean-Francois Witz, Jean Meriaux

# Mechanisms of incursion accommodation during interaction between a vibrating blade and an abradable coating

Romain Mandard [a,b,c,e,*], Yannick Desplanques [a,b,c], Grégory Hauss [a,c], Jacky Fabis [d], Jean-François Witz [a,c], Jean Meriaux [e]

[a] Univ Lille Nord de France, F-59000 Lille, France
[b] ECLille, LML, F-59650 Villeneuve d'Ascq, France
[c] CNRS, UMR 8107, F-59650 Villeneuve d'Ascq, France
[d] ONERA, The French Aerospace Lab, F-59000 Lille, France
[e] SNECMA, site de Villaroche, F-77550 Moissy-Cramayel, France

Abradable materials are used as inner coatings in aeronautical compressors. In the event of blade–casing interaction, the abradable coating accommodates the incursion of the blade tip in order to protect the blade and the casing from severe damage. In this study, an experiment was conducted in conditions representative of the full-scale situation in terms of velocity, temperature and the dynamical characteristics of blades. The mechanisms of incursion accommodation were investigated based on dynamical data and a *post mortem* analysis of the coating and the wear debris. First, dynamical blade tip incursion was estimated by considering blade vibrations and coating waviness. The tip incursion was found to be significantly different from the measured displacement of the blade foot. Next, a *post mortem* analysis of the coating was performed at the surface and sub-surface. Four mechanisms were identified, namely debris release, surface shearing, compaction and reversible deformation. Care was taken to provide orders of magnitude for the different mechanisms relating to residual thickness loss of the coating.

## 1. Introduction

Minimizing the in-service clearance between rotating blades and the surrounding casing has been shown to improve the efficiency of aeronautical compressors. In fact, it may well be critical to blade and casing integrity in the event of contact between the two. Indeed, during engine operation, the rotor–stator interface is subjected to centrifugal rotor loadings, differential thermal expansions between the rotor and the stator as well as accelerations arising from aircraft maneuvering and vibrations. Abradable materials are used for the inner coatings of casings in order to accommodate blade incursions. Blade strikes lead to coating wear and blade vibrations, which occur simultaneously. Experimental investigations on full-scale compressors have demonstrated the existence of an association between the excited blade modes and the wear profile of abradable coatings [1] that leads to blade failure. In order to predict the vibratory response of blades induced by rubs against the casing, a large number of numerical models have been developed [2–6]. In other models, wear laws have been implemented to simulate the behavior of the abradable material when rubbed by the blade [7–10]. Different basic assumptions are made in these models. Marscher [7] has proposed a model based on the presence of a shear mix layer at the blade–coating interface. In the model by Williams [8], the wear depth is considered to be zero below a certain load and proportional to the radial load above this threshold. In their model, Legrand et al. [9] consider that the behavior of the abradable material is controlled by a two-region constitutive law that includes both elastic and plastic parameters. Salvat et al. [10] developed a model based on an analogy between abradable removal and milling, in which wear has been modeled as the removal of chips. In order to validate these wear models or define their scope of validity, experimental research is required.

Different kinds of experiments have been developed to identify the wear mechanisms pertaining to abradable materials. The test rig at Sulzer-Innotec [11,12] is capable of generating interactions for a wide range of tangential speeds (up to 400 m $s^{-1}$) and temperatures (up to 1000 °C). Dadouche et al. [13] studied the effect of speed, incursion rate and temperature on rubbed surfaces and correlated these parameters with the tangential cutting force. More recently, Fois et al. [14,15] investigated the relationship between incursion rates, wear mechanisms and interaction forces for an abradable AlSi-hBN coating at relative velocities of 100–200 m $s^{-1}$. The authors highlighted two main mechanisms, namely cutting

* Corresponding author at: Univ Lille Nord de France, F-59000 Lille, France.
*E-mail address:* romain.mandard@centraliens-lille.org (R. Mandard).

**Nomenclature**

| | |
|---|---|
| $x$ | coordinate along the normal direction (mm) |
| $y$ | coordinate along the tangential direction (mm) |
| $V_T$ | tangential speed of the abradable coating (m s$^{-1}$) |
| $T_a$ | temperature of the abradable coating (°C) |
| $V_e$ | electrical pulse sent to the actuator (V) |
| $\Phi$ | angular position of the coated cylinder (°) |
| $R$ | radius of the coated cylinder (mm) |
| $D_N$ | apparent incursion (displacement of the blade foot in the normal direction) (μm) |
| $\Delta_N$ | variation of apparent incursion (blade foot stroke during interaction) (μm) |
| $D_T$ | blade bending displacement (mm), measured at 17.5 mm from the blade tip |
| $f_N/f_N^{max}$ | normal component of the blade–coating interaction force (–) |
| $f_T/f_T^{max}$ | tangential component of the blade–coating interaction force (–) |
| $\delta$ | incursion of the blade tip into the abradable coating (μm) |
| $p_b$ | position of the blade tip (μm) |
| $p_a$ | position of the abradable coating (μm) |
| $L$ | blade length (mm) |
| $\alpha_1$ | modal amplitude of the first blade bending mode (mm) |
| $Z_1$ | mode shape of the first blade bending mode (–) |
| $w$ | coating waviness (μm) |
| $R_f$ | radius of the median filter used for image post-processing (px) |
| $S$ | threshold used for image post-processing (gray level) |
| $p$ | percentage of porosity in the abradable coating (–) |
| $p_0$ | initial percentage of porosity in the abradable coating (–) |
| $\Delta e$ | variation of thickness due to coating compaction (μm) |
| $l_d$ | debris length (μm) |
| $\Delta l_d$ | variation of debris length (μm) |
| $h_d$ | average thickness of wear debris (μm) |
| $e_d$ | coating thickness evacuated as debris (μm) |

(high incursion rate) and adhesive transfer (low incursion rate). The coating-to-blade tip transfer was investigated by means of a stroboscopic imaging technique, that enabled the transfer growth to be recorded during the interaction. *Post mortem* observations showed an association between adhesive transfer and grooving of the coating, which is consistent with Borel's analysis on worn service parts [16]. These test rigs and experiments [11,13–15] can provide wear maps of abradable coatings, in which the dominant wear mechanisms are generally expressed as a function of the tangential blade speed and incursion rate.

However, in the quoted studies, the wear analysis of abradable coatings is often confined to macroscopic observations and descriptions of worn surfaces, which limits the possibilities for developing physical wear laws in the abovementioned numerical models. The interpretation of interaction scenarios is complex since wear mechanisms are analyzed after many blade rubs. Cuny et al. [17] developed a test setup that uses a gas gun to launch an abradable AlSi-polyester specimen into interaction with a cutting tool. Single-pass incursions were generated, but the wear mechanisms were not investigated and only room-temperature experiments were conducted. On the whole, the test rigs have been designed with small rigid blades and therefore do not investigate the relationships between blade vibrations and abradable coating wear.

The present paper aims to propose a different experimental approach for studying the accommodation of blade incursion in an abradable coating. The test rig, presented in papers [18–20], is capable of reproducing very short blade–seal interactions. The blade–seal configuration has been simplified with respect to the full-scale case to enable comprehensive instrumentation. The experiments are representative of low-pressure compressor conditions in terms of the materials used (abradable AlSi-polyester material, titanium blade), the relative rotor–stator speed (up to 95 m s$^{-1}$), the abradable coating temperature (up to 300 °C) and the dynamical characteristics of the blade. In this study, we did not investigate a wide range of interaction conditions but instead concentrated our efforts on performing a detailed analysis of a single-pass interaction between a vibrating blade and an abradable AlSi-polyester coating. This involved estimating the interaction force and blade tip incursion by taking into account the blade vibrations. Additionally, the mechanisms of incursion accommodation were investigated at the surface and sub-surface by means of high-speed imaging, SEM and X-ray microtomography.

## 2. Blade–coating interaction

### 2.1. Test rig

The configuration and instrumentation of the test rig, developed at ONERA, the French Aerospace Lab, have been discussed in detail in previous papers [19,20]. As shown in Fig. 1a, the test rig consists of a rotating cylinder (300 mm in diameter) whose external surface is coated with an abradable material. The relative blade/coating speed $V_T$ is generated by spinning the cylinder. The interaction is generated by translating the blade toward the abradable coating. In order to do this, the titanium blade is fastened to a small rigid unit, which is moved in direction $x$ by means of a piezo-electric actuator (Fig. 1b). The translation of this small rigid unit (i.e. translation of the blade foot) is defined as the apparent incursion $D_N$. The blade used in this study has a simplified geometry but with flexural characteristics representative of compressor blades [20]. In order to reach in-service compressor temperatures, the coating is heated by an induction heating system (Fig. 1a). The surface temperature $T_a$ of the abradable coating is monitored via an infrared pyrometer that is properly calibrated to take into account the emissivity.

The instrumentation has been chosen to capture the dynamics of blade–seal interactions of a few milliseconds. The apparent incursion $D_N$, which results from the electrical command sent to the actuator and the interaction force, is measured with laser displacement sensor 2 (Fig. 1b). A second sensor, displacement sensor 1, measures the blade bending displacement $D_T$ (in direction $y$) at 17.5 mm from the blade tip. $D_T$ is used to estimate the tangential component of the interaction force at the blade tip, $f_T$. A piezoelectric force sensor is placed between the actuator and the small rigid unit to measure the incursion force in direction $x$. The acceleration of the small rigid unit in direction $x$ is measured by means of two accelerometers. The output signals of the force sensor and the accelerometers are post-processed to estimate the normal component of the interaction force $f_N$. The method used to estimate the interaction force has been described previously in [20]. Images of the interaction are recorded using a high-speed camera placed on one side of the test rig. The blade bending motion and the ejection of wear debris are both captured by the camera at 12 500 frames/s with a resolution of $1024 \times 1024$ pixels. On the opposite side of the incursion cell, a third sensor, laser displacement sensor 3, is used to record the circumferential profile of the coating. Two types of acquisitions are performed

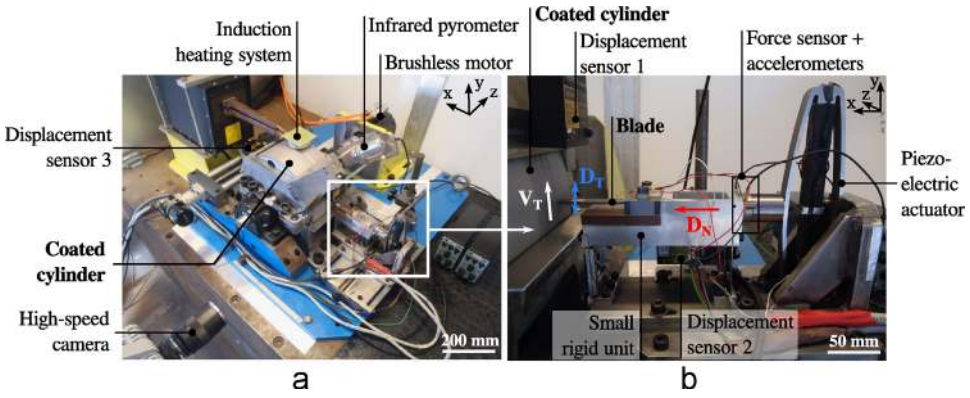


**Fig. 1.** (a) Overview and (b) closer view of the incursion cell of the test rig.

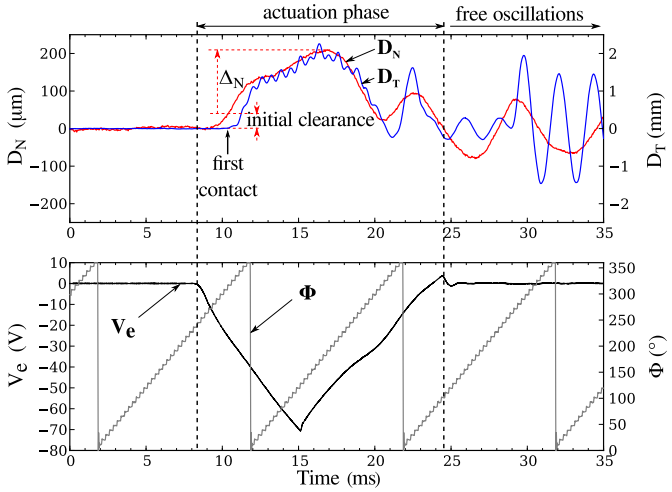


**Fig. 2.** Raw signals obtained in the experiment: electrical pulse $V_e$ sent to the actuator, angular position of the cylinder $\Phi$, apparent incursion $D_N$ and blade bending displacement $D_T$ measured at 17.5 mm from the blade tip.

with this sensor. The first type is a low-speed scan: the coating is scanned at a low rotational speed before and after interaction with the blade in order to evaluate the circumferential wear profile. The second type is an *in situ* measurement: the circumferential profile is measured during the interaction in order to identify the radial position of the coating at the time of impact. This *in situ* measurement is used to estimate the dynamical blade tip incursion $\delta$.

### 2.2. Dynamical data

The present study aims to investigate the mechanisms of incursion accommodation in conditions representative of the full-scale situation: tangential relative speed $V_T = 92\ \mathrm{m\ s^{-1}}$ and abradable coating temperature $T_a = 280\ ^\circ\mathrm{C}$. Before launching the blade–coating interaction, a running-in phase was carried out at a very low tangential speed ($V_T = 1\ \mathrm{m\ s^{-1}}$) at room temperature, in order to ensure rubbing over the whole width of the blade tip. At the end of this running-in period, the blade was moved backward with the actuator to set the initial blade–coating clearance; allowance was made for thermal expansion of the cylinder during heating. Then, the cylinder was set into rotation at the test speed and the coating was heated simultaneously. When the test temperature and speed were reached, a trigger switched off the heating system (to avoid distortion of acquisition signals) and applied an electrical pulse $V_e$ to the actuator in order to generate the interaction.

The raw signals recorded during the experiments are shown in Fig. 2. The experiment can be divided into two phases. The first one corresponds to the period when the command $V_e$ was relayed to the actuator, namely the actuation phase. Upon first contact, the maximum stroke of the blade foot toward the coating was $\Delta_N = 170\ \mu\mathrm{m}$. The second phase corresponds to the free-oscillation stage experienced by the incursion cell, i.e. when no voltage was applied to the actuator. The vibratory characteristics of the incursion cell were responsible for oscillations in displacement $D_N$, which led to a few isolated contact occurrences within the free-oscillation phase. The vibratory characteristics of the incursion cell and the nature of any resulting contact have been discussed in a previous paper [19]. An encoder embedded in the brushless motor recorded the angular position $\Phi$ of the cylinder (Fig. 2). This enabled us to match dynamical data with spatial positions on the coating and was particularly useful for pinpointing where the coating was rubbed by a single-pass of the blade or impacted more than once. For the purpose of this study, the abradable coating will be analyzed at locations where the blade struck once.

#### 2.2.1. Interaction force

The tangential and normal components of the blade–coating interaction force ($f_T$ and $f_N$ respectively) were estimated according to the method presented in [20] and are plotted in Fig. 3. During the actuation phase, the force experienced appreciable variations that reflected variations in the contact conditions during the interaction. During the free-oscillation phase, contact occurred on two occasions, as suggested by the blade bending displacement $D_T$ (cf. Fig. 2).

#### 2.2.2. Blade tip incursion

In the literature, abradable coatings are usually characterized by setups that involve small rigid blades; this allows us to equate the incursion of the blade tip into the coating with the stroke of the blade foot or the abradable specimen. In the present study, however, the blade tip incursion $\delta$ and the blade foot displacement (apparent incursion $D_N$) are not equal, because of the blade vibrations. Moreover, the circumferential profile of the coating indicates a wavy surface that is likely to influence blade tip incursion $\delta$. In view of the above, the respective positions of the blade tip and the abradable coating are estimated through an analytical calculation. The position of the blade tip $p_b$ in direction $x$ expressed as a function of time is given by

$$p_b(t) = D_N + \int_0^L \cos\left(\alpha_1(t)\frac{dZ_1}{ds}\right) ds - L + b\sin\left(\alpha_1(t)\frac{dZ_1}{ds}(L)\right) \qquad (1)$$

where $D_N$ is the apparent incursion, $\alpha_1$ is the modal amplitude of the first blade bending mode, $Z_1$ is the mode shape of the first blade bending mode and $L$ is the blade length. The position of the abradable

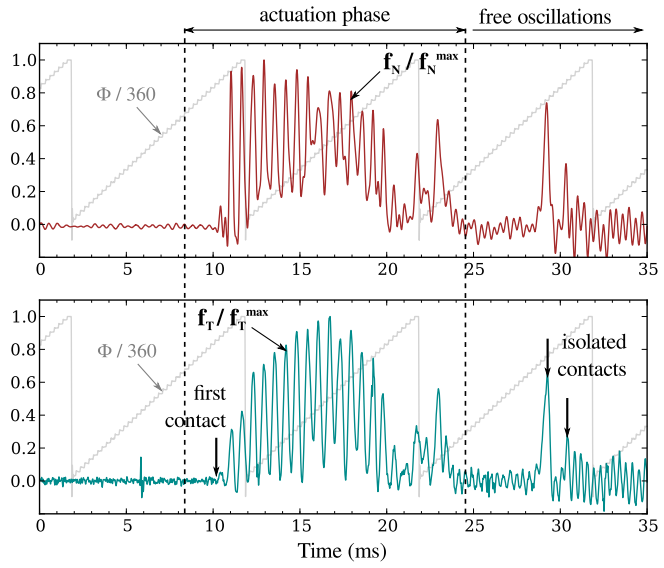


**Fig. 3.** Normalized components of the interaction force ($f_N$=normal, $f_T$=tangential).

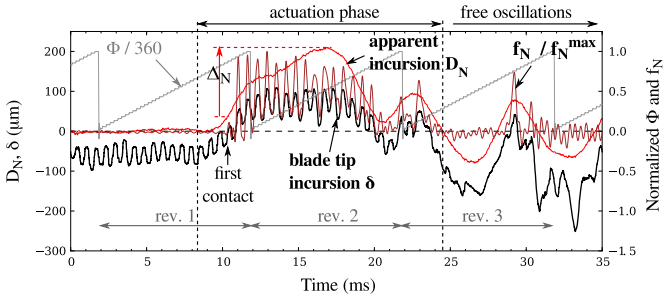


**Fig. 4.** Estimated blade tip incursion $\delta$, with apparent incursion $D_N$ and normal interacting force $f_N$ (normalized).

coating facing the blade tip is expressed as

$$p_a(t) = \frac{1}{2R}\left(\alpha_1(t)Z_1(L) - b\cos\left(\alpha_1(t)\frac{dZ_1}{ds}(L)\right)\right)^2 - w(t) \quad (2)$$

where $R$ is the cylinder radius and $w$ is the coating waviness. The quantities $D_N$ and $w$ were measured during the experiment. In this estimation, the flexural displacement of the blade is approximated by applying the Euler–Bernoulli beam model in the first mode, while $\alpha_1$ was measured through the displacement $D_T$. Details about this calculation and the measurement of $w$ are available in Appendix A. The blade tip incursion $\delta$ is finally given by

$$\delta(t) = p_b(t) - p_a(t) \quad (3)$$

The incursion $\delta$ is plotted as a function of time in Fig. 4. Negative values of $\delta$ correspond to a clearance between the blade tip and the abradable coating while positive values correspond to a penetration of the blade tip into the coating. The initial coating waviness of approximately 60 μm in amplitude can be observed in the incursion $\delta$ before the actuation phase. Then, the incursion $\delta$ resulting from the blade vibrations and the coating profile evolves in phase with the normal force $f_N$. It is worth nothing that the blade tip incursion $\delta$ is significantly different from the apparent incursion $D_N$ in terms of both amplitude and shape. The maximum values of blade tip incursion are on the order of $\delta = 100$ μm, while the blade foot stroke is $\Delta_N = 170$ μm.

### 2.3. Wear profile

In order to evaluate the circumferential wear profile, the abradable coating was scanned with laser displacement sensor 3

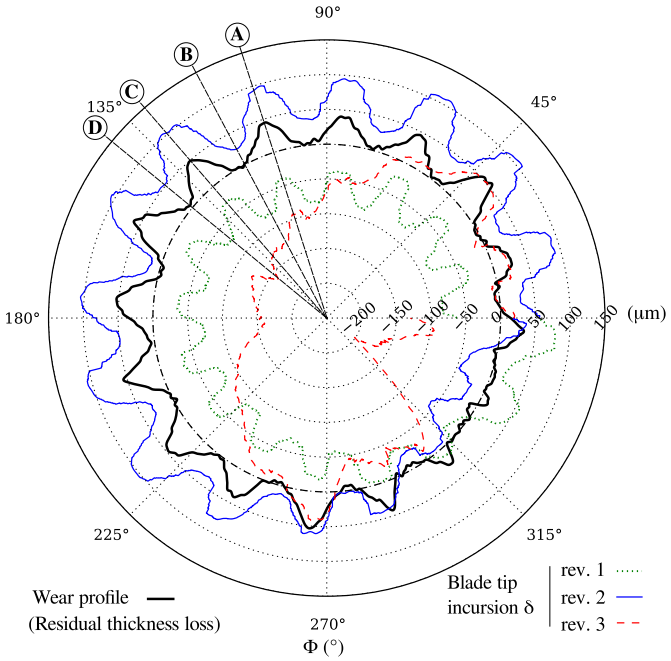


**Fig. 5.** Wear profile of the abradable coating and blade tip incursion $\delta$ for revolutions 1, 2 and 3 (for revolution numbering, see Fig. 4).

(cf. Fig. 1a) at a low rotational speed before and after the interaction. Three profiles were measured: in the center, on the left side and on the right side of the experimental track. Details about the measurement and post-processing of data have been published in [20]. The average circumferential wear profile is shown in Fig. 5 as a function of the angular position $\Phi$ of the cylinder. This wear profile corresponds to the residual thickness loss of the coating. In this figure, the blade tip incursion is divided into three cylinder revolutions 1, 2 and 3 highlighted in Fig. 4 to enable comparisons with the wear profile. Since the actuation phase lasted longer than one cylinder revolution (cf. Fig. 2) and contact occurred during the free-oscillation phase, some locations on the coating were impacted more than once. In order to simplify the analysis of wear, these locations were not studied. By contrast, the angular interval 90–225° was rubbed only once by the blade. An examination of this angular interval clearly shows that the blade tip incursion here is greater than the residual thickness loss of the coating. At local maxima of $\delta$ ($\approx 100$ μm), the thickness loss is approximately 50 μm. At local minima of $\delta$ ($\approx 50$ μm), the thickness loss was found to be close to zero. This comparison between the blade tip incursion and the wear profile suggests that the abradable coating accommodated a part of the incursion by reversible deformation. The other part of the incursion, corresponding to the residual thickness loss, was accommodated by permanent deformation and/or material removal. The mechanisms associated with such residual thickness loss are investigated in the following section.

## 3. Methods for the analysis of accommodation mechanisms

### 3.1. Sample selection

During the interaction, the force and the tip incursion experienced significant variations on the scale of the millisecond (Fig. 4). From these data, four successive times that were representative of the variations in the incursion conditions were selected. The corresponding angular positions were identified on the coating to enable subsequent material analysis. As shown in Figs. 5 and 3, positions A and C correspond to local maxima of incursion ($\delta \approx 100$ μm),

thickness loss ( $\approx 50$ µm) and force ($f_T/f_T^{max} = 0.9, f_N/f_N^{max} = 0.9$). By contrast, positions B and D are local minima for incursion ($\delta \leq 50$ µm), thickness loss ( $\approx 0$ µm) and force ($f_T/f_T^{max} \leq 0.2$, $f_N/f_N^{max} \leq 0.5$). The abradable coating was sectioned at positions A, B, C and D, indicated in Fig. 6. In the $z$ direction, the samples are slightly larger than the track width (9 mm); in the tangential direction $y$, they measure 10 mm and are centered on the angular position $\Phi$ given in Fig. 5. As mentioned above, a running-in was conducted before the interaction. A representative sample R of the coating after this running-in period was also sectioned from another experimental track.

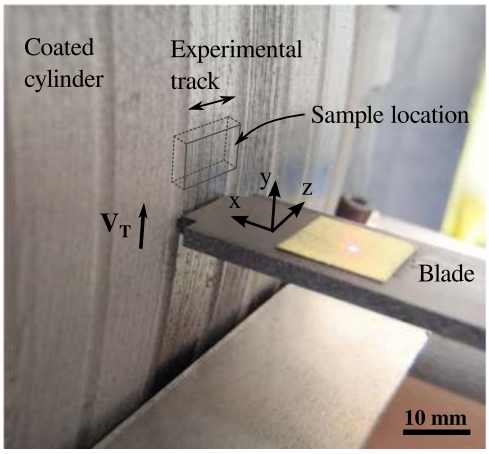


**Fig. 6.** Location of abradable coating samples.

### 3.2. Coating surface analysis

The rubbed surfaces of the selected samples were analyzed by means of Scanning Electron Microscopy (SEM), using both secondary and back-scattered electrons. Back-scattered electrons were particularly useful for highlighting the metallic AlSi phase and the polyester. Prior to SEM observations, the surfaces were gold coated to prevent charging of the polyester during scanning by the electron beam.

### 3.3. Coating compaction

As abradable materials often have porous microstructures, they may accommodate incursion by compaction, otherwise known as densification [11,15,21]. In the present work, the compaction mechanism was defined as the loss of porosity in the coating and investigated by means of X-ray microtomography [23]. X-ray microtomography is a non-invasive porosity evaluation technique and does not require any sectioning, polishing or chemical attack that could modify the porosity [24]. The samples were scanned with a voxel size of 2 µm. After performing a volume reconstruction, 2D slices were extracted, as presented in Fig. 7 (sample A). The grayscale images represent X-ray attenuation maps where the three phases of the abradable material are distinguishable thanks to the shades of gray. As indicated in Fig. 7a, the metallic AlSi phase is represented by the highest gray levels (highest X-ray attenuation coefficient), the polyester phase by intermediate levels and porosity

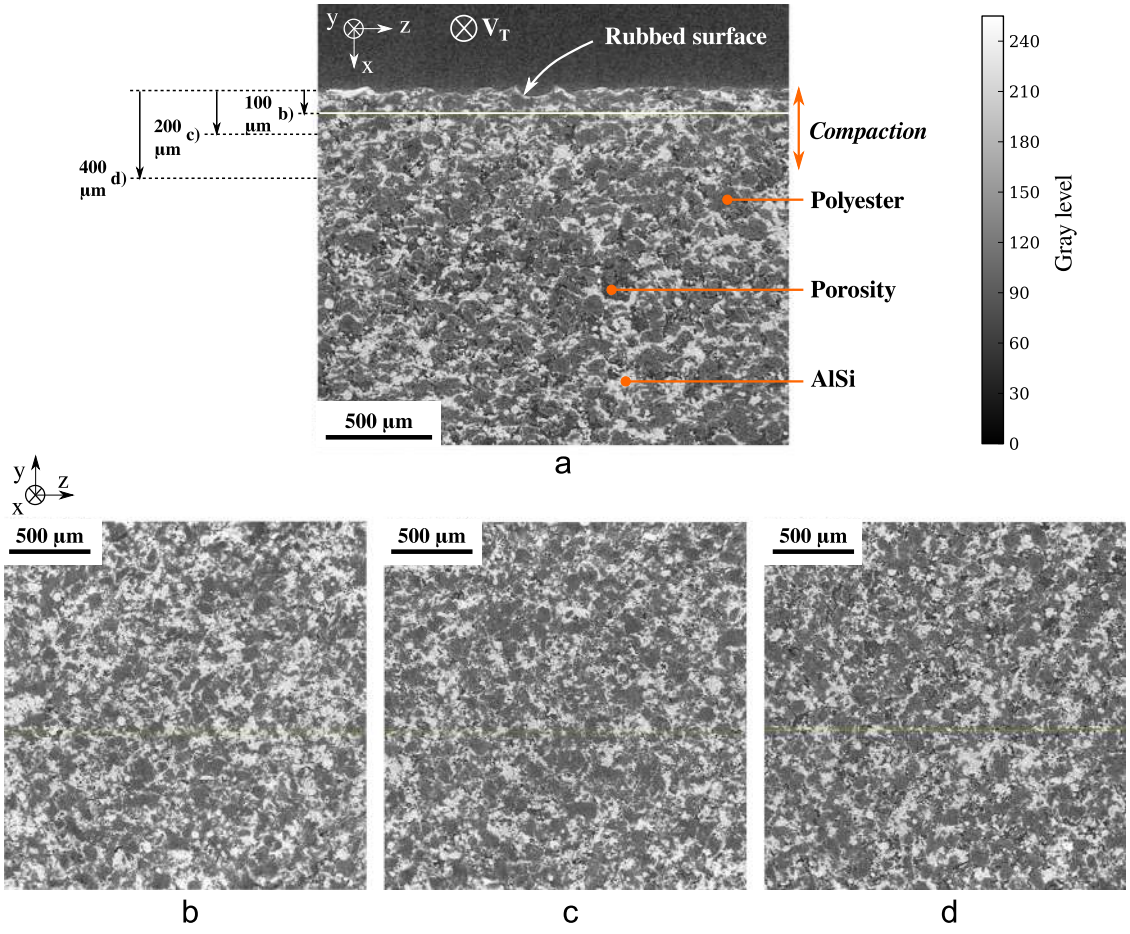


**Fig. 7.** Images of the abradable coating obtained by X-ray tomography (1 vx = 2 µm): (a) slice orthogonal to tangential speed $V_T$ and ($yz$) slices at (b) 100 (c) 200 and (d) 400 µm from the rubbed surface.

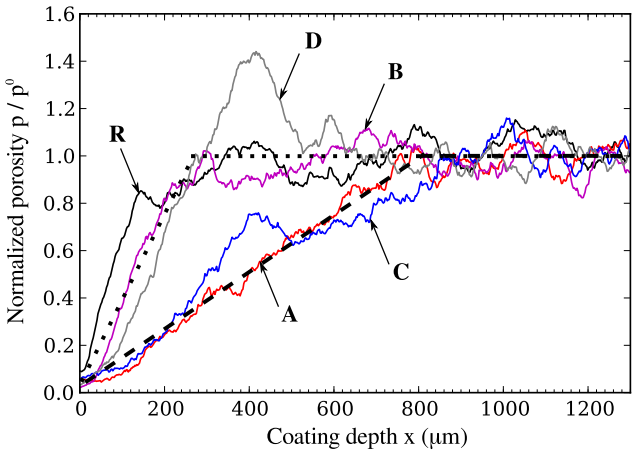


**Fig. 8.** Porosity (normalized) as a function of coating depth ($x=0$ corresponds to the rubbed surface) for samples A, B, C, D and R.

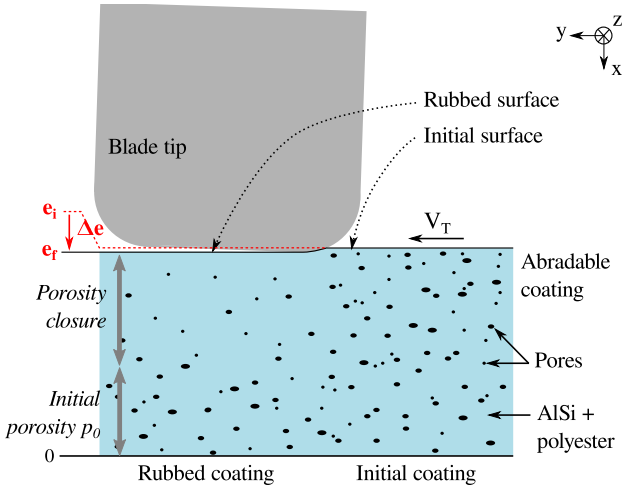


**Fig. 9.** Schematic description of abradable coating compaction induced by a blade rub.

(air) by the lowest levels. The slice shown in Fig. 7a is orthogonal to the tangential speed $V_T$. An observation of the near-surface region indicates that the coating was compacted, i.e. porosities were closed. It is difficult to estimate the depth affected by compaction based on this slice alone. Thus, ($yz$) slices were extracted at 100, 200 and 400 µm from the rubbed surface, as shown in Fig. 7b, c and d respectively. A comparison between these three images shows that porosity (represented by dark pixels) increases with distance from the rubbed surface $x$. We propose to take this analysis further with image processing in order to give an indicator of compaction and compare the samples.

### 3.3.1. Evaluation of the normal porosity profile

According to Fig. 7, the coating seems to have been gradually affected by compaction in the normal direction $x$. For each sample, the set of ($yz$) slices obtained by tomography (with a 2-µm step) were analyzed in order to determine the porosity profile along the normal direction. First, a procedure consisting in the alignment of histogram peaks was applied to the five scans (A, B, C, D and R) by using an affine transformation of the gray levels. This enabled us to compare the five scans in terms of gray levels. Second, the images were filtered by means of a median filter of radius $R_f=3$ px. Third, the images were thresholded (threshold $S=93$) to isolate the porosity. A test image was used to identify the most suitable parameter set ($R_f$, $S$). The filtering and thresholding stages applied to the reference image are presented in Appendix B. Although the choice of a threshold is subjective, the same set of parameters was applied to all the samples so that the porosity percentages obtained could be compared to each other.

Fig. 8 shows the porosity evaluated in the five samples as a function of the coating depth $x$, where $x=0$ corresponds to the rubbed surface. In all the samples, porosity is close to zero at the rubbed surface and increases in a near-linear fashion up to the initial porosity $p_0$. From a certain depth, the porosity levels off at approximately $p_0$. The transition point between the linear slope and the constant regions varies between samples, and compaction is clearly related to the incursion conditions. Indeed, for samples A and C corresponding to local maxima of incursion and force (cf. Fig. 3), the transition occurs at approximately $x=800$ µm. By contrast, for samples R (running-in), D and B (local minima for incursion and force) the transition occurs at approximately $x=250$ µm. The curve corresponding to sample D shows a high porosity level between 250 and 500 µm, that is attributed to an initial local defect in the coating.

### 3.3.2. Compaction calculation

This sections aims to calculate the thickness loss $\Delta e$ of the coating induced by sub surface compaction so that compaction can be interpreted in relation to the measured thickness loss (Fig. 5). As Fig. 9 shows, $\Delta e$ is considered to be the difference between the initial coating thickness $e^i$ and the coating thickness after compaction $e^f$:

$$\Delta e = e^i - e^f \tag{4}$$

It is assumed here that compaction of the abradable coating only arises from porosity closure. The porosity in the initial state (i.e. after thermal spraying and surface machining) is considered to be uniform throughout the material: $p=p_0$. As observed in Fig. 8, after the running-in phase and the blade–coating interaction, the porosity becomes dependent on the distance from the surface $x$: $p=p(x)$. The displacement $\Delta e$ is expressed as (for calculation details, see Appendix C):

$$\Delta e = \frac{p^0}{1-p^0}\left(e^f - \int_0^{e^f} \frac{p(x)}{p^0}\,dx\right). \tag{5}$$

## 3.4. Wear debris

In the literature, wear characterization of abradable coatings is usually based on the analysis of rubbed specimens. Although some authors have provided information about the nature of debris, such as size, shape and direction of ejection [11,21,22], detailed analyses remain rare. Recently, Fois et al. [14] proposed a dynamical tracking approach for measuring the rate at which debris was transferred from an abradable AlSi-hBN coating to the blade tip. In the present section, we examine in detail the debris released as a result of contact. This is achieved by means of high-speed imaging and a *post mortem* analysis (SEM and X-ray microtomography).

### 3.4.1. Analysis of debris release by high-speed imaging

As mentioned in Section 2.1, images were captured at 12.5 frames/ms during the blade–coating interaction. A portion of an image is presented in Fig. 10a and shows a side view of the contact between the blade tip and the abradable coating. During the actuation phase of the interaction (cf. Fig. 4), debris from the abradable material was continuously formed and released. The images of the interaction were used to evaluate the length change of the debris. As shown in Fig. 10b, the debris size was approximated by an equivalent skeleton of two segments. The skeleton length $l_d$, defined as the apparent length of the debris, was determined frame by frame. The apparent length $l_d$ is plotted in

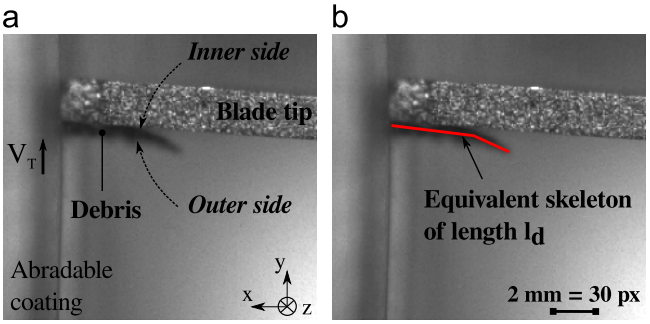


**Fig. 10.** High-speed imaging of the interaction: (a) wear debris and (b) definition of apparent length $l_d$.

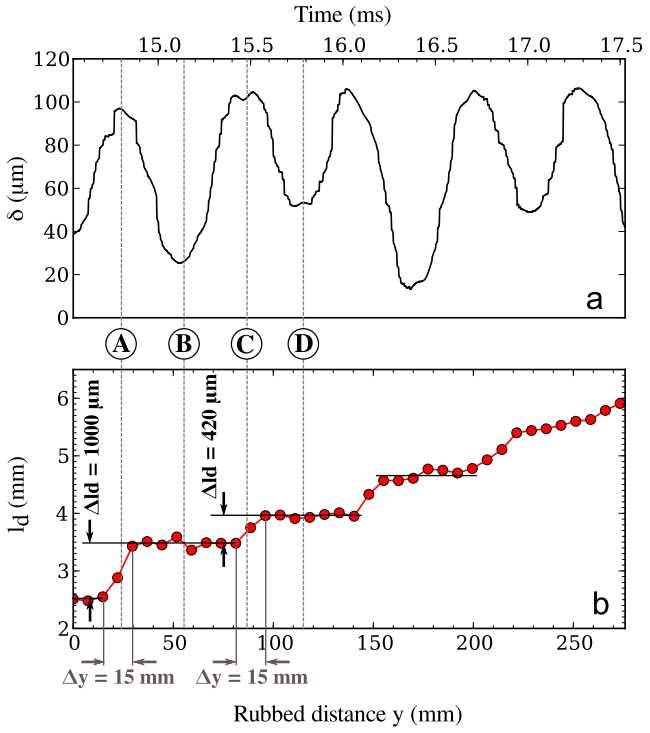


**Fig. 11.** Evolution of (a) blade tip incursion $\delta$ and (b) the apparent length $l_d$ of the wear debris during revolution 2.

Fig. 11 as a function of time and rubbed distance. Only data corresponding to the time interval in which the measurement could be made with confidence have been included. Indeed, for shorter debris lengths, the method was not accurate enough and for longer lengths, the debris had started to twist. The times corresponding to samples A, B, C and D described in Section 3.1 are found in the time interval of Fig. 11 and have been highlighted. According to this figure, the evolution of the debris length correlates with the blade tip incursion $\delta$. The debris length increases when the incursion is maximal and remains relatively unchanged when the incursion is minimal. During the intervals surrounding positions A and C, the debris length increases by $\Delta l_d = 1000\,\mu m$ and $\Delta l_d = 420\,\mu m$, respectively. The distance of coating rubbed during these periods of debris growth is $\Delta y = 15$ mm at both positions A and C. The values of $\Delta l_d$ and $\Delta y$ were used to estimate the thickness of the coating that was evacuated as debris.

### 3.4.2. Post mortem observations of wear debris

The debris shown in Fig. 10a was trapped in order to carry out morphological and microstructural analysis. Particular care was taken to differentiate between the inner and outer sides of the debris (cf. Fig. 10a), as they were likely to have different characteristics. Observations of the inner and outer debris sides were carried out by using Scanning Electron Microscopy. The average thickness of the debris $h_d$ was determined by means of X-ray microtomography.

### 3.4.3. Estimation of coating thickness evacuated as debris

For positions A and C, knowing the increase in debris length $\Delta l_d$ (Fig. 11), the corresponding rubbed distance $\Delta y$ (Fig. 11) and the average thickness of the debris $h_d$, it is possible to give an estimation of the coating thickness that was evacuated as debris ($e_d$). Applying the conservation of volume yields

$$e_d = \frac{h_d \Delta l_d}{\Delta y}. \tag{6}$$

## 4. Results

A set of dynamical data (force, incursion, debris release) was collected and a *post mortem* analysis (coating, released debris) performed in order to interpret how blade tip incursion was accommodated by the abradable coating in conditions representative of the full-scale situation (tangential speed $V_T = 92\ m\ s^{-1}$, coating temperature $T_a = 280\ °C$). Four samples (A, B, C and D) corresponding to successive angular positions in the rubbing process were selected for a thorough analysis (cf. Fig. 5). Sample R representing the coating after the running-in period (i.e. before dynamical interaction) was also analyzed for use as a reference. Fig. 12 shows the rubbed surfaces of samples R, A (maximum incursion) and B (minimum incursion). These images were obtained by means of SEM with back-scattered electrons and enabled us to clearly differentiate the metallic AlSi phase (white regions) from the polyester phase (black regions). The running-in surface (Fig. 12a) is characterized by a clear distinction between these two phases, indicating that cutting wear was the predominant mechanism. By contrast, the polyester in sample A (Fig. 12b) shows signs of having experienced plastic flow. On the surface of sample B (Fig. 12c), only a very small amount of polyester flow is observed, suggesting that the rubbing process was much less severe at this time. Another hypothesis is that this small amount of polyester was transferred by the blade from site A to site B. It should be noted that the images of samples A (Fig. 12b) and B (Fig. 12c) were captured at the same position in direction $z$, i.e. across the track width (cf. Fig. 6).

Images of sample A at a higher magnification are presented in Fig. 13. The temperature of the experiment, $T_a = 280\ °C$, was chosen to be close to the melting point of the thermoplastic polymer (liquid crystal polyester) used in the abradable material. Heat and the interaction force caused the polyester on the surface to stretch plastically in the tangential direction. The metallic AlSi phase was sheared and dislodged as particles of a few tens of microns, some of which became trapped in the polyester threads.

The structure of the wear debris was also investigated by means of SEM. Fig. 14a and b shows the outer side of the debris while Fig. 14c and d shows the inner side. The *inner* and *outer* sides were defined in Fig. 10a. According to this figure, the outer side corresponds to the free surface of the coating and was not in contact with the blade during the interaction. The two sides have different morphologies. The inner side indicates a smooth surface with a high proportion of polyester (Fig. 14c), presumably resulting from plastic flow along the leading edge of the blade. By contrast, the outer surface is wrinkled, as shown in Fig. 14a. This observation is in agreement with the measured lengths $\Delta l_d$ (increase in debris length) and $\Delta y$ (corresponding rubbed distance) highlighted in Fig. 11. During a phase of debris release, $\Delta y$ was one order of magnitude greater than $\Delta l_d$. Detached metallic particles measuring

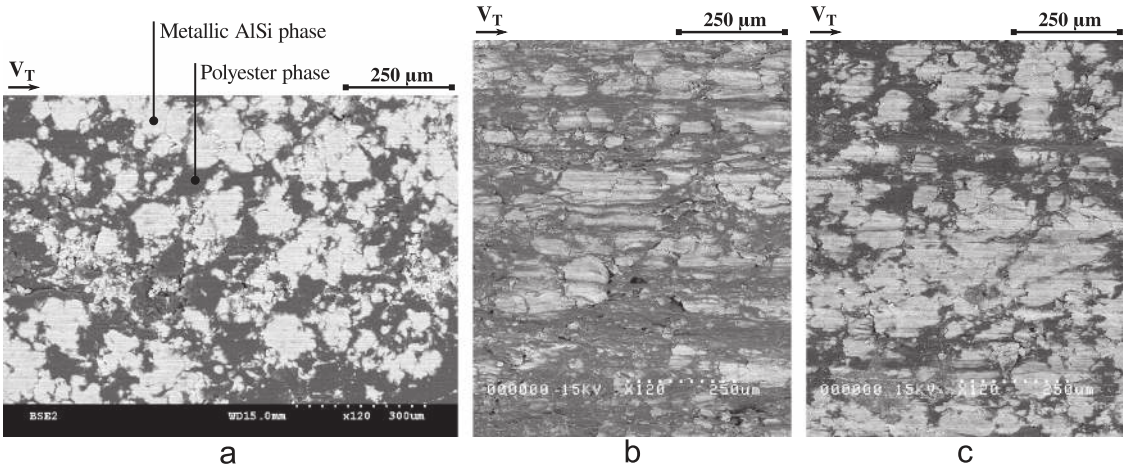


**Fig. 12.** SEM observations of rubbed surfaces: (a) sample R (running-in), (b) sample A (max. incursion) and (c) sample B (min. incursion).

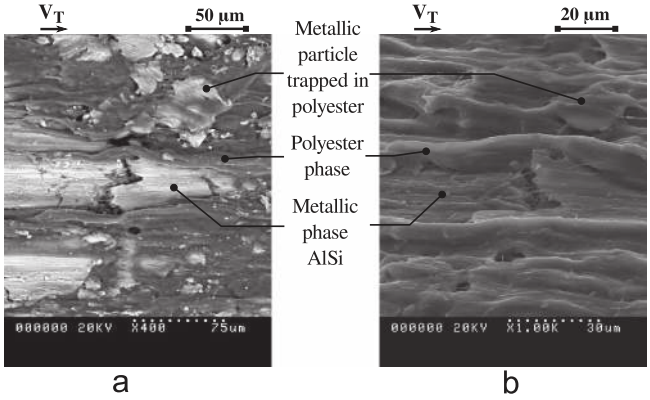


**Fig. 13.** Rubbed surface of sample A (max. incursion) observed by SEM (a) at medium magnification with back-scattered electrons, and (b) at high magnification with secondary electrons and tilted sample.

a few micrometers in thickness were found in the debris (Fig. 14b). Since the debris material did not pass through the contact, these particles are characteristic of the coating after the running-in phase.

In order to evaluate the debris thickness $h_d$, a part of the debris was cut and scanned by X-ray microtomography at a resolution of 1 µm. An $(xy)$ slice of the reconstructed volume is shown in Fig. 15. The axes $x$ and $y$ were defined in Fig. 10 and the $(xy)$ plane corresponds to the plane of the high-speed images that were recorded. Thus, both the inner and the outer sides as well as the characteristic wrinkles of the debris are visible in Fig. 15. According to this tomographic scan, the average thickness of the debris $h_d$ is on the order of 150 µm. Using Eq. (6), we estimated the thickness of the coating $e_d$ that was evacuated as debris during the intervals surrounding positions A and C (Fig. 11).

The numerical results for the evacuated thickness $e_d$ are given in Table 1, which also includes other data measured or estimated for the four samples, namely the tangential and normal components of the interacting force, $f_T$ and $f_N$ respectively (cf. Section 2.2.1), the blade tip incursion $\delta$ (cf. Section 2.2.2), the coating compaction $\Delta e$ (cf. Section 3.3) and the measured thickness loss (cf. Section 2.3). In the calculation of compaction $\Delta e$, the contribution of the preliminary running-in stage was subtracted from the results obtained for samples A, B, C and D. Although exact values have been given in Table 1, it is important to note that these values should be interpreted as orders of magnitude. During the interaction, at positions A and C (Fig. 5), the blade tip incursion and the tangential and normal forces reached local maxima on the order of $\delta = 100$ µm, $f_T/f_T^{max} = 0.9$ and $f_N/f_N^{max} = 0.9$, respectively. At these sites, the measured thickness loss depth is approximately 50 µm. This indicates that the incursion was accommodated by both reversible and permanent deformation. Permanent deformation was associated with coating compaction, debris release and surface shearing. The sum of compaction (a few tens of micrometers) and coating thickness evacuated as debris (a few micrometers) corresponds – in order of magnitude – to the residual thickness loss. At sites B and D, the forces and the incursion reached local minima: $\delta \leq 50$ µm, $f_T/f_T^{max} \leq 0.2$ and $f_N/f_N^{max} \leq 0.5$. The residual thickness loss was found to be practically zero, which is consistent with the estimation of near-zero compaction. According to Fig. 11, the wear debris did not experience any growth. Moreover, there is very little evidence of surface shearing (Fig. 12c), which is consistent with the very low tangential forces. These observations suggest that at sites B and D, the blade tip incursion was accommodated only by reversible deformation. It is interesting to note that the wear debris formed as a single piece despite a halt in its growth at positions B and D, suggesting that the debris adhered to the blade tip during the rubbing process. This was later confirmed by the *post mortem* analysis of the blade tip, on which abradable material consisting of stretched polyester and AlSi particles was found (Fig. 16).

In view of these elements, a schematic description of the accommodation mechanisms is proposed. This is shown in Fig. 17, where the scale and configuration apply to the blade–coating system presented in this paper. A blade tip incursion of 100 µm is represented, in accordance with estimations at sites A and C (cf. Fig. 5). According to the previous observations, the blade tip incursion and relative speed are accommodated by four main mechanisms. These mechanisms can be defined according to the concept of three-body contact and the related third-body flows introduced by Godet [25] and Berthier [26].

The first mechanism consists in the formation of wear debris at the leading edge of the blade, which constitutes the wear flow and can be interpreted as the result of two source flows of third body. The first source flow corresponds to the brittle separation of the superficial layer from the bulk coating at the leading edge of the blade. This layer becomes wrinkled (cf. Fig. 14a and b) to accommodate the sudden change of velocity of the material. Indeed, the wear debris is evacuated in a direction approximately orthogonal to the tangential speed $V_T$ (cf. Fig. 10). This first source flow forms the outer side of the debris. The second source flow of third body arises from the shearing of the abradable material in the vicinity of the leading edge. A part of the second source flow is evacuated along the leading edge and forms the inner side of the debris, while the other part feeds the contact and constitutes a thin sheared film at the blade–coating interface. This film, or internal flow of third body, is indicated by the plastic polyester flow and the detachment of flat

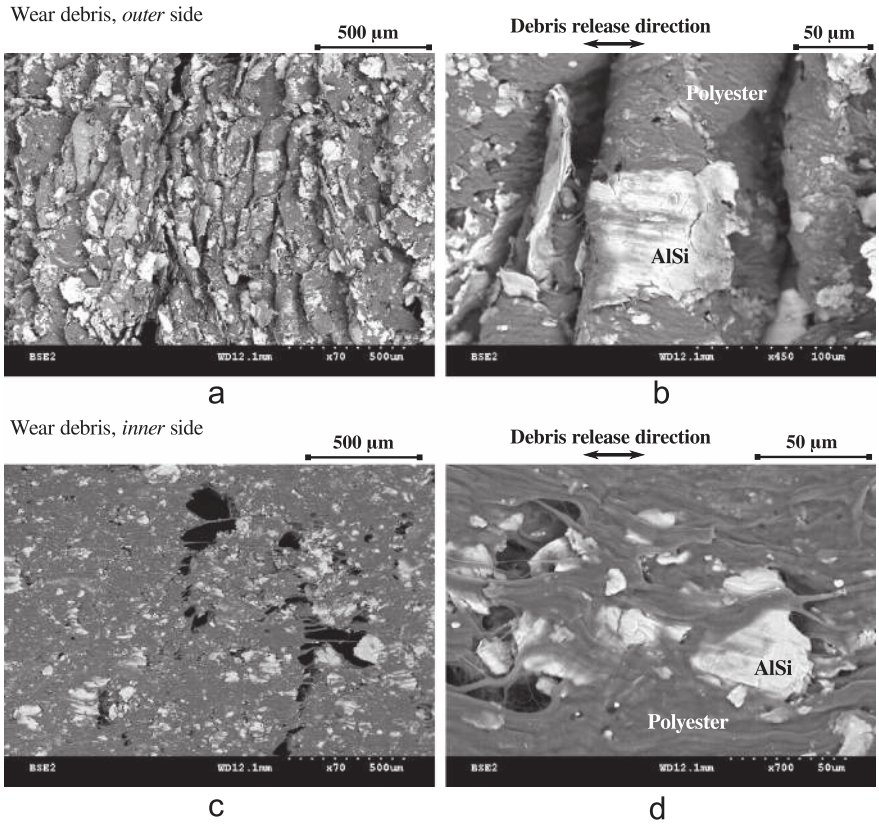


**Fig. 14.** Wear debris: (a) and (b) outer side (low and high magnification respectively); (c) and (d) inner side (low and high magnification respectively). SEM observations with back-scattered electrons. For the definition of *outer* and *inner*, refer to Fig. 10.

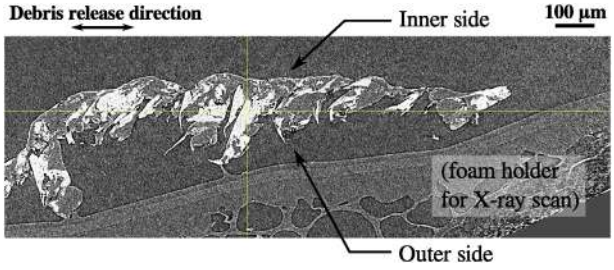


**Fig. 15.** (*xy*) slice of a sample of wear debris, obtained by X-ray tomography (resolution: 1 vx = 1 µm). For *x*- and *y*-axes, refer to Fig. 10.

**Table 1**
Summary of the dynamical and *post mortem* data corresponding to samples A, B, C and D shown in Fig. 5.

| Measured data | Site A | Site B | Site C | Site D |
|---|---|---|---|---|
| Tangential force $f_T/f_T^{max}$ | 0.9 | 0 | 0.9 | 0.2 |
| Normal force $f_N/f_N^{max}$ | 0.9 | 0.2 | 0.9 | 0.5 |
| Blade tip incursion $\delta$ (µm) | 97 | 26 | 104 | 52 |
| Compaction $\Delta e$ (µm) | 42 | 2 | 37 | (−4) |
| Thickness evacuated as debris $e_d$ (µm) | 10 | 0 | 4 | 0 |
| Residual thickness loss (µm) | 45 | 0 | 50 | 5 |

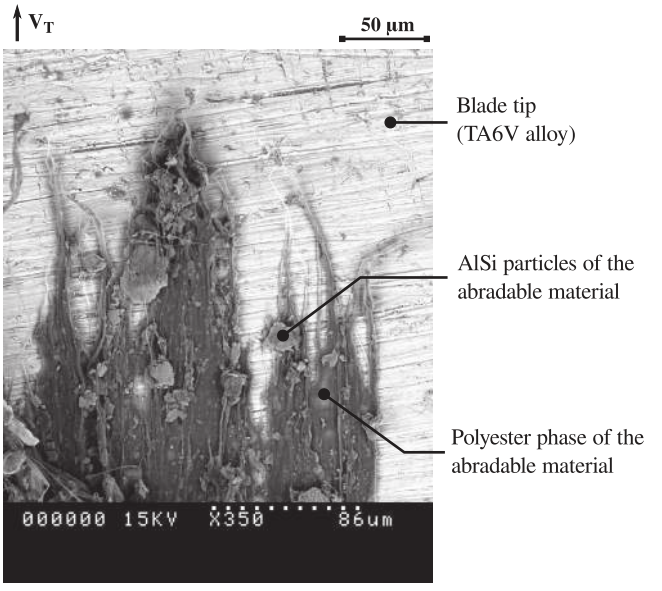


**Fig. 16.** Transfer of abradable material onto the blade tip (SEM observation, back-scattered electrons).

AlSi particles at the surface (Fig. 13) and corresponds to the second accommodation mechanism. The internal flow of third body accommodates the difference of velocity between the two first bodies, which are the blade and the abradable coating in the present case. This description is in agreement with the analytical model by Marscher [7]. In this model, which is based on experimental observations, the relative blade–coating velocity is accommodated by a shear mix layer in which recirculating plastic flow occurs.

The third mechanism that we identified is coating compaction, which is associated with porosity closure (Fig. 8). Debris release and compaction were found to be responsible for residual thickness loss of the abradable coating. The fourth mechanism is an accommodation of a part of the incursion by reversible deformation, as evidenced by the observation that the estimated blade tip incursion is greater than the measured thickness loss (Table 1). According to the data

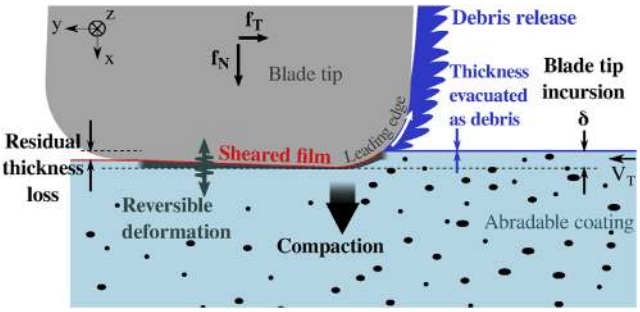


**Fig. 17.** Accommodation of blade tip incursion by the abradable coating.

estimated at sites B and D (Table 1), low incursion is mostly accommodated by reversible deformation. This observation is consistent with the wear laws of Williams [8] and Legrand et al. [9], in which the existence of an elastic region or a load threshold is assumed.

It is worth noting that the present experimental results are difficult to compare with those found in the literature as the mechanisms occurring at full-scale temperature and speed are still not fully understood and have not been studied in the case of a flexible blade. In most of the experiments conducted thus far, blade tip incursion has been monitored through the displacement of an abradable specimen toward a rigid rotating blade. The incursions generated are on the order of a few tenths of micrometers per pass [12–14], which is several orders of magnitude lower than the incursion depths encountered in the present study. In the present case, which is more representative of full-scale conditions in terms of blade dynamics and temperature, blade tip incursion has been shown to be related to blade vibrations. The incursion has also been correlated with the initial waviness of the coating (Fig. 4). The latter is somewhat reflective of the full-scale situation, as compressor coating profiles are never perfectly circular because of the way in which casings are mounted or as a result of previous blade rubs [1].

## 5. Conclusion

In this study, interaction between a blade and an abradable coating was generated at a speed and temperature representative of in-service conditions in aeronautical compressors. This interaction was analyzed in detail in order to identify the mechanisms of incursion accommodation. The interaction force and the blade tip incursion were estimated from indirect measurements by considering the blade bending kinematics. The wear mechanisms of the abradable AlSi-polyester material were investigated by means of a *post mortem* analysis of the coating as well as dynamical and *post mortem* analyses of wear debris release. Four mechanisms have been identified: debris release, surface shearing, compaction by porosity closure and reversible deformation. According to our results, the loss of thickness due to debris release and compaction is of the same order of magnitude as the residual thickness loss of the coating. Surface shearing occurs and may be observed through the presence of a plastic-flow film of polyester in the sliding direction and dislodged AlSi particles of a few tens of micrometers. Reversible deformation can be deduced from the difference between the incursion and the residual thickness loss. These mechanisms correlate with the incursion depth and interaction force, which vary on the scale of the millisecond during interaction. Indeed, among the four samples that were analyzed, release of debris, compaction and surface shearing are activated at incursion/force maxima while incursion/force minima are mainly accommodated by reversible deformation.


## Acknowledgements

This study was supported by SNECMA and funded by the French Ministry of Higher Education and Research, both of whom we gratefully acknowledge. Thanks are also due to the International Campus on Safety and Intermodality in Transportation (CISIT), the Nord-Pas-de-Calais Region, the European Community, the Regional Delegation for Research and Technology, and the National Centre for Scientific Research.


## Appendix A. Estimation of blade tip incursion

The incursion of the blade tip into the abradable coating, $\delta$, is considered to be the difference between the respective positions of the blade tip and the abradable coating. The blade foot displacement, or apparent incursion $D_N$, is measured by means of a displacement sensor. However, due to blade vibrations, foot and tip displacements are not equal and blade kinematics must be taken into account in the calculation of the tip position $p_b$. The position $p_a$ of the abradable coating facing the blade is also subject to variations during the interaction because of the initial waviness of the coating. The method used to estimate the incursion $\delta = p_b - p_a$ is detailed in the following.

### A.1. Blade tip position, $p_a$

Contributions to the blade tip displacement in direction $\vec{u}$ are (cf. Fig. A1):

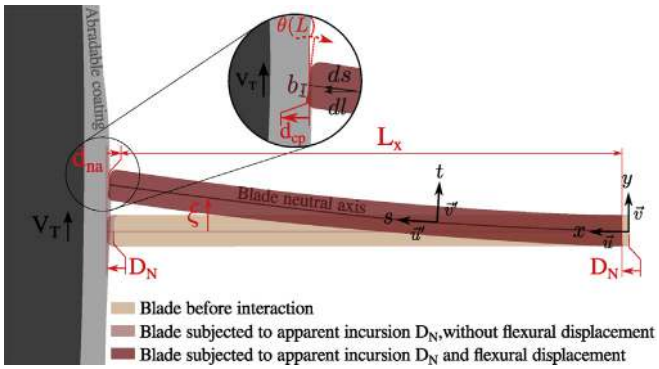


**Fig. A1.** Schematic description of the blade tip position.

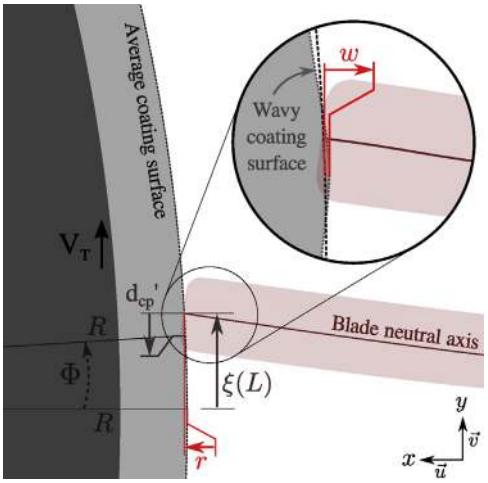


**Fig. A2.** Schematic description of the coating position.

- apparent incursion $D_N$, or blade foot displacement, measured by means of laser displacement sensor 2 (Fig. 1);
- displacement $d_{na}$ of the blade tip on the neutral axis induced by blade length conservation during bending;
- displacement $d_{cp}$ of the contact point induced by the rotation of the blade tip $\theta(L)$.

Therefore, the current position of the blade tip is expressed as (zero being taken to be the blade tip position before interaction):

$$p_b = D_N + d_{na} + d_{cp}. \tag{A.1}$$

*A.1.1. Calculation of displacement $d_{na}$*

$$d_{na} = L_x - L \tag{A.2}$$

where $L$ is the blade length and $L_x$ is the projected length of the neutral axis of the blade along $\vec{u}$. $d_{na}$ is a function of time since it varies with the flexural displacement during the interaction. The blade is modeled according to the Euler–Bernoulli beam theory with clamped–free boundary conditions [19]. The flexural displacement $\xi(x,t)$ is approximated by the first mode:

$$\xi(x,t) = \alpha_1(t) Z_1(x) \tag{A.3}$$

where $Z_1$ is the first mode shape of the Euler–Bernoulli beam and $\alpha_1$ is the corresponding modal amplitude. $\alpha_1$ is measured via the displacement $D_T$:

$$D_T(t) = \xi(x_f, t) = \alpha_1(t) Z_1(x_f) \tag{A.4}$$

Rotations of blade sections $\theta$ are assumed to have small values but the coordinate systems $(\vec{u}, \vec{v})$ and $(\vec{u}', \vec{v}')$ do not coincide. An infinitesimal element $dl$ of $L_x$ is given by

$$dl = \cos(\theta)\, ds \tag{A.5}$$

with

$$\theta = \frac{\partial \xi}{\partial s} \tag{A.6}$$

The projected length $L_x$ is obtained after integration of $dl$ over the blade length ($s \in [0, L]$):

$$L_x = \int_0^L dl \tag{A.7}$$

$$L_x = \int_0^L \cos\left(\frac{\partial \xi}{\partial s}\right) ds \tag{A.8}$$

which yields

$$d_{na} = \int_0^L cos\left(\frac{\partial \xi}{\partial s}\right) ds - L. \tag{A.9}$$

*A.1.2. Calculation of displacement $d_{cp}$*

According to Fig. A1, $d_{cp}$ is given by

$$d_{cp} = b \sin(\theta(L)) \tag{A.10}$$

$$d_{cp} = b \sin\left(\frac{\partial \xi}{\partial s}(L)\right) \tag{A.11}$$

where the distance $b$ is half the blade tip thickness.

*A.1.3. Final expression*

Combining Eqs. (A.1) and (A.3) allows us to express the blade tip position $p_b(t)$ as:

$$p_b(t) = D_N + \int_0^L \cos\left(\alpha_1(t)\frac{dZ_1}{ds}(s)\right) ds - L + b \sin\left(\alpha_1(t)\frac{dZ_1}{ds}(L)\right) \tag{A.12}$$

*A.2. Abradable coating position $p_a$*

The position $p_a$ of the abradable coating facing the blade is the difference between (Fig. A2):

- the gap $r$ induced by the curvature of the cylinder and blade bending;
- and the coating waviness $w$ measured during the experiment by means of laser displacement sensor 3, as shown in Fig. A3.

$p_a$ is written as

$$p_a = r - w. \tag{A.13}$$

*A.2.1. Calculation of gap r*

The gap $r$ is calculated from the following trigonometric equations:

$$\sin \Phi = \frac{\xi(L) - d'_{cp}}{R} \tag{A.14}$$

$$\cos \Phi = \frac{R - r}{R} \tag{A.15}$$

where $R$ is the cylinder radius, and

$$d'_{cp} = b \cos\theta(L) \tag{A.16}$$

Eqs. (A.14) and (A.15) yield ($1 = \sin^2(\Phi) + \cos^2(\Phi)$):

$$1 = \left[\frac{\xi(L) - b\cos\theta(L)}{R}\right]^2 + \left[\frac{R-r}{R}\right]^2 \tag{A.17}$$

Assuming that $|r| \ll R$, a first-order development yields

$$r = \frac{1}{2R}\left(\xi(L) - b\cos\theta(L)\right)^2 \tag{A.18}$$

$$r = \frac{1}{2R}\left(\xi(L) - b\cos\left(\frac{\partial \xi}{\partial s}(L)\right)\right)^2 \tag{A.19}$$

$$r = \frac{1}{2R}\left(\alpha_1 Z_1(L) - b\cos\left(\alpha_1 \frac{dZ_1}{ds}(L)\right)\right)^2. \tag{A.20}$$

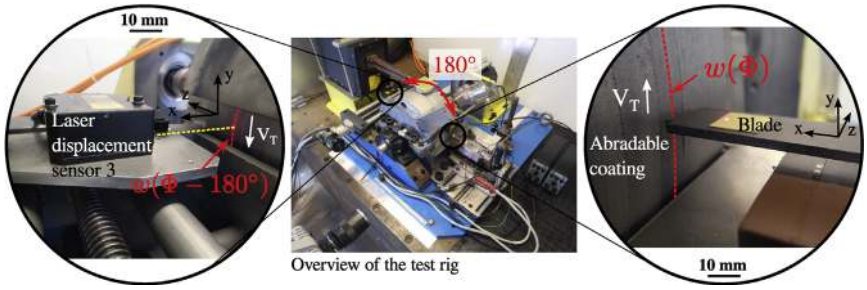


**Fig. A3.** *In situ* measurement of the coating waviness.

*A.2.2. Measurement of coating waviness w*

The coating waviness $w$ was measured by means of laser displacement sensor 3, as shown in Fig. A3. The sensor was placed at the rear of the test rig with a 180° angular offset from the interaction. The raw signal was post-processed by taking into account the angular offset and the sensor response time, thus giving $w(\Phi)$, where $\Phi$ is the angular position of the rotating cylinder.

*A.2.3. Final expression*

With Eq. (A.3), the position $p_a$ of the abradable coating is given by

$$p_a(t) = \frac{1}{2R}\left(\alpha_1(t)Z_1(L) - b\cos\left(\alpha_1(t)\frac{dZ_1}{ds}(L)\right)\right)^2 - w(t) \tag{A.21}$$

*A.3. Blade–coating incursion δ*

Finally, the incursion $\delta$ can be estimated through the following equation:

$$\delta(t) = D_N(t) + \int_0^L \cos\left(\alpha_1(t)\frac{dZ_1}{ds}(s)\right) ds - L + b\sin\left(\alpha_1(t)\frac{dZ_1}{ds}(L)\right) - \frac{1}{2R}\left(\alpha_1(t)Z_1(L) - b\cos\left(\alpha_1(t)\frac{dZ_1}{ds}(L)\right)\right)^2 - w(t)\Bigg) \tag{A.22}$$

where $D_N$ (apparent incursion) and $w$ (coating waviness) are measured during the interaction by means of laser displacement sensors and the modal amplitude $\alpha_1$ is measured via the flexural displacement $D_T$.

## Appendix B. Post-processing of the images obtained by X-ray microtomography

The slices obtained by X-ray microtomography were post-processed in two steps in order to estimate the porosity. First, raw images (Fig. B1a) were filtered using a median filter of radius $R_f = 3$ px. The filtered images (Fig. B1b) were then thresholded at a value of $S = 93$. An example of a thresholded image is shown in Fig. B1d. Porosity is represented by black pixels. Fig. B1c presents the thresholded image without any filtering. A comparison between Fig. B1a and c clearly shows that in the absence of filtering, porosity is overestimated because of the noise contained in the image.

## Appendix C. Calculation of compaction

The following equations refer to Fig. 9. Let $\Delta y$ be a length of coating in the tangential direction, and $\Delta z$ be a length of coating along the blade width. In the initial state $i$ (before interaction), the percentage of porosity is considered to be uniform throughout the coating: $p = p_0$. The volume $\Delta y \Delta z e^i$ is the sum of the material (AlSi + polyester) volume $V_m^i$ and the porosity volume $V_p^i$:

$$\Delta y \Delta z e^i = V_m^i + V_p^i \tag{C.1}$$

$$\Delta y \Delta z e^i = V_m^i + p^0 \Delta y \Delta z e^i \tag{C.2}$$

In the final state $f$, the volume $\Delta y \Delta z e^f$ is the sum of the material volume $V_m^f$ and the porosity volume $V_p^f$:

$$\Delta y \Delta z e^f = V_m^f + V_p^f \tag{C.3}$$

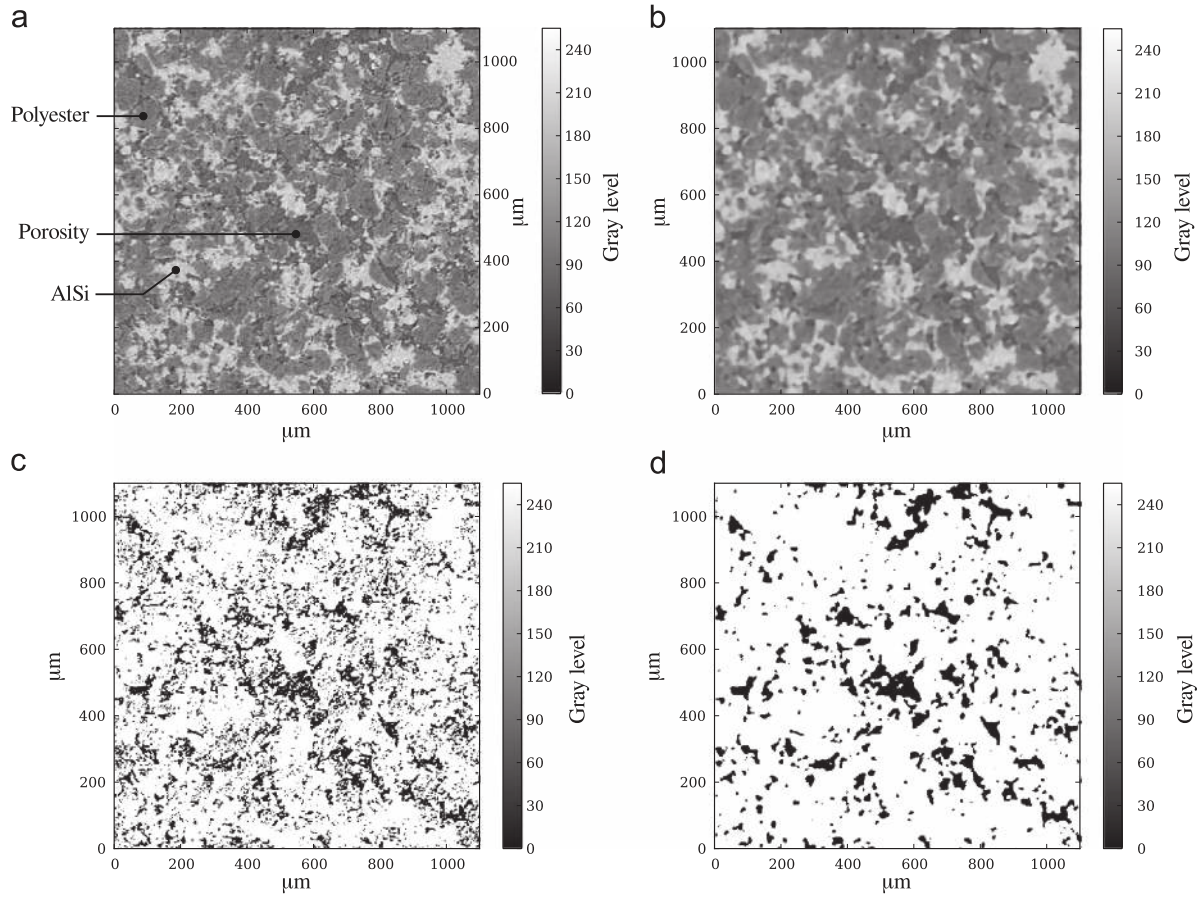


**Fig. B1.** Post-processing of tomographic images: (a) raw image (b) filtered-only image (c) thresholded-only image (d) filtered and thresholded image (parameters $R_f = 3$ px, $S = 93$).

Only the volume of porosity is changed by the interaction while the material volume remains the same:

$$V_m^f = V_m^i \tag{C.4}$$

$$V_m^f = (1-p^0)\Delta y \Delta z e^i \quad \text{according to Eq. (C.2)} \tag{C.5}$$

The final volume of porosity is obtained by integrating the porosity profile $p(x)$:

$$V_p^f = \iiint_{\Delta y \Delta z e^f} p(x)\, dx\, dy\, dz \tag{C.6}$$

$$V_p^f = \Delta y \Delta z \int_0^{e^f} p(x)\, dx \tag{C.7}$$

Eqs. (C.3), (C.5) and (C.7) yield

$$\Delta y \Delta z e^f = (1-p^0)\Delta y \Delta z e^i + \Delta y \Delta z \int_0^{e^f} p(x)\, dx \tag{C.8}$$

$$\Delta y \Delta z e^f = (1-p^0)\Delta y \Delta z (e^f + \Delta e) + \Delta y \Delta z \int_0^{e^f} p(x)\, dx \tag{C.9}$$

$$e^f = (1-p^0)(e^f + \Delta e) + \int_0^{e^f} p(x)\, dx \tag{C.10}$$

And finally

$$\Delta e = \frac{p^0}{1-p^0} \left( e^f - \int_0^{e^f} \frac{p(x)}{p^0}\, dx \right). \tag{C.11}$$

## References


[1] A. Millecamps, J.-F. Brunel, P. Dufrenoy, F. Garcin, M. Nucci, Influence of thermal effects during blade—casing contacts experiments, in: Proceedings of the ASME IDETC/CIE, August 30–September 2, 2009, San Diego, CA, USA.

[2] A. Kascak, The Response of Turbine Engine Rotors to Interference Rubs, NASA Technical Report No. 80-C-14, 1980.

[3] J. Padovan, F. Choy, Nonlinear dynamics of rotor/blade/casing rub interactions, ASME J. Turbomach. 109 (1987) 527–534.

[4] Z.C. Feng, X.Z. Zhang, Rubbing phenomena in rotor–stator contact, Chaos Soliton. Fract. 14 (2002) 257–267.

[5] S.K. Sinha, Non-linear dynamic response of a rotating radial Timoshenko beam with periodic pulse loading at the free end, Int. J. Nonlinear Mech. 40 (2005) 113–149.

[6] S.K. Sinha, Rotordynamic analysis of asymmetric turbofan rotor due to fan blade-loss event with contact-impact rub loads, J. Sound Vib. 332 (2013) 2253–2283.

[7] W.D. Marscher, A phenomenological model of abradable wear in high performance turbomachinery, Wear 59 (1980) 191–211.

[8] R.J. Williams, Simulation of blade casing interaction phenomena in gas turbines resulting from heavy tip rubs using an implicit time marching method, in: Proceedings of the ASME Turbo Expo 2011, Vancouver, Canada.

[9] M. Legrand, A. Batailly, C. Pierre, Numerical investigation of abradable coating removal in aircraft engines through plastic constitutive law, ASME J. Comput. Nonlinear Dyn. 7 (2012).

[10] N. Salvat, A. Batailly, M. Legrand, Modeling of abradable coating removal in aircraft engines through delay differential equations, ASME J. Eng. Gas Turbine Power 135 (2013).

[11] R.K. Schmid, New High Temperature Abradables for Gas Turbines (Ph.D. thesis), Swiss Federal Institute of Technology, Zurich, Switzerland, 1997.

[12] M. Bounazef, S. Guessasma, B. Ait Saadi, The wear, deterioration and transformation phenomena of abradable coating BN-SiAl-bounding organic element, caused by the friction between the blades and the turbine casing, Mater. Lett. 58 (2004) 3375–3380.

[13] A. Dadouche, M.J. Conlon, W. Dmochowski, B. Liko, J.P. Bedard, Experimental evaluation of abradable seal performance at high temperature, in: Proceedings of the ASME Turbo Expo 2008, June 9–13, Berlin, Germany.

[14] N. Fois, J. Stringer, M.B. Marshall, Adhesive transfer in aero-engine abradable linings contact, Wear 304 (2013) 202–210.

[15] N. Fois, M. Watson, J. Stringer, M.B. Marshall, An investigation of the relationship between wear and contact force for abradable materials, Proc. Inst. Mech. Eng. Part J.-J. Eng. Tribol. 229 (2) (2015) 136–150.

[16] M.O. Borel, A.R. Nicoll, H.W. Schläpfer, R.K. Schmid, The wear mechanisms occurring in abradable seals of gas turbines, Surf. Coat. Technol. 39/40 (1989) 117–126.

[17] M. Cuny, S. Philippon, P. Chevrier, F. Garcin, Experimental measurement of dynamic forces generated during short-duration contacts: application to blade–casing interactions in aircraft engines, Exp. Mech. 54 (2014) 101–114.

[18] S. Baïz, J. Fabis, X. Boidin, Y. Desplanques, Experimental investigation of the blade/seal interaction, Proc. Inst. Mech. Eng. Part J.-J. Eng. Tribol. 227 (9) (2013) 980–995.

[19] R. Mandard, J.F. Witz, Y. Desplanques, J. Fabis, J. Meriaux, Wavelet analysis of experimental blade vibrations during interaction with an abradable coating, ASME J. Tribol. 136 (2014).

[20] R. Mandard, J.F. Witz, X. Boidin, J. Fabis, Y. Desplanques, J. Meriaux, Interacting force estimation during blade/seal rubs, Tribol. Int. 82 (2015) 504–513.

[21] J. Wolak, A.F. Emery, S. Etemad, S.R. Choi, Blade tip geometry – a factor in abrading sintered seal material, ASME J. Tribol. 106 (1984) 527–533.

[22] R.C. Bill, D.W. Wisander, Friction and Wear of Several Compressor Gas-path Seal Materials, NASA Technical Paper No. 1128, 1978.

[23] L. Salvo, P. Cloetens, E. Maire, S. Zabler, J.J. Blandin, J.Y. Buffière, W. Ludwig, E. Boller, D. Bellet, C. Josserond, X-ray micro-tomography an attractive characterisation technique in materials science, Nucl. Instr. Methods Phys. Res. Sec. B 200 (2003) 273–286.

[24] J. Matejicek, K. Blahoslav, J. Dubsky, K. Neufuss, N. Hopkins, J. Zwick, Alternative methods for determination of composition and porosity in abradable materials, Mater. Charact. 57 (2006) 17–29.

[25] M. Godet, The third-body approach: a mechanical view of wear, Wear 100 (1984) 437–452.

[26] Y. Berthier, Background on friction and wear, Handbook of Material Behavior Models, 2001, pp. 676–699.